Ultrasonics Sonochemistry 120 (2025) 107418

Contents lists available at ScienceDirect

Ultrasonics Sonochemistry

journal homepage: www.elsevier.com/locate/ultson

Numerical simulation of a continuous sonoreactor for cotton cellulose residues recovery

Pierre Dal [a], Julie Kring [c], Dalma Schieppati [a], Daria C. Boffito [a,b,*,1]

[a] Polytechnique Montréal, Dept. Chemical Engineering, CP 6079, Succ CV, Montréal, QC H3C 3A7, Canada
[b] Canada Research Chair in Engineering Process Intensification and Catalysis (EPIC), Polytechnique Montreal, Canada
[c] Khepra Inc., 5760 Arboretum Drive, Los Altos, CA 94024, USA

ARTICLE INFO

Keywords:
Ultrasound
Biomass
Acoustic cavitation
Numerical simulation
Sonochemical reactor

ABSTRACT

Numerical simulations are a tool for sonoreactors design and reaction parameters choice. We modeled a sonoreactor with six lateral flat transducers along the walls and a concentric high intensity focused ultrasound (HIFU) transducer at the bottom. We examined the effects of the gap between the reflector and transducers (h), cone radii in the lower part and ultrasound frequency (f) on the cavitation activity of cellulose esters solutions. Then, we investigated the effects of the properties of cellulose solutions on the cavitation activity. The simulation accounts for the attenuation due to the cavitation bubbles and considers the propagation of sound waves from the HIFU as linear. We measured the speed of sound in a cellulose esters solutions and included it in our simulations: 1545 m s^{-1} for 6.25 g L^{-1}. h, f, the density (ρ) and the viscosity (μ) of the cellulose solutions have the most significant effects – accounting for 34 % to 61 % of the variance – on the total acoustic pressure (p_T) and active cavitation surface area (V). p_T and V increase as f and ρ increase, and as h and μ decrease. At 78 kHz and h = 0.075 m, with $\mu = 5.3 \times 10^{-3}$ Pa.s and $\rho = 941.8$ kg m^{-3}, the simulation resulted in the highest p_T and largest V: 1.96×10^6 Pa and 3.99×10^{-2} m^2. These data provide a basis to optimize sonoreactor design and operating conditions for enhanced cavitation performance in cellulose processing.

1. Introduction

Process intensification (PI) is a transformative approach in chemical engineering aimed at increasing the energy efficiency and sustainability of chemical processes. PI encompasses a variety of strategies and breakthrough technologies that lower the energetic expenditure by 20 % to 80 %, decrease reagents consumption by 10 to 1000 times, and dramatically (Table 1) reduce the size of the equipment (100 times) [1,2]. Ultrasound (US) is one of the notable tools in PI, and it has gathered significant attention due to its unique capabilities and benefits, which include the reduction of energy consumption and decrease of the equipment's size [3]. US is a mechanical wave that consists of successive acoustic cycles of compression (positive pressure) and rarefaction (negative pressure). Compression pushes molecules together, while rarefaction pulls molecules apart. In the rarefaction phase, if the pressure amplitude exceeds the tensile strength of the liquid, vapor-filled cavitation bubbles will form. Pure liquids have a high tensile strength and do not cavitate [4]. However, liquids that are impure – i.e. containing particles and bubbles – have lower tensile strength and cavitate more easily. After bubbles formation, stable cavitation or transient cavitation arises [4,5]. Stable cavitation arises at low intensity (< 0.05 W cm^{-2} at 20 kHz), whereas transient cavitation arises at high intensity (> 0.1 W cm^{-2} at 20 kHz) [5–7]. During stable cavitation bubbles grow slowly, while during transient cavitation bubbles grow rapidly from dozens or hundreds of times their equilibrium radius before collapsing in less than a microsecond [8]. The collapse of cavitation bubbles originates microjets and localized hotspots of temperature up to 5000 K and pressure up to 500 atm [4], thereby eliciting both physical and chemical effects on the sonicated system. Reactive species form at the liquid – gas interface of the bubbles and inside the bubbles [9]. The transient cavitation in water, cleaves the oxygen – hydrogen bonds, leading to the formation of reactive hydroxyl radicals. For example, at 52 kHz and 1.5 atm each bubble generates 6.6×10^5 hydroxyl radicals, and has a maximum bubble radius of 28.9 μm [10]. The sonication of N,N-dimethylacetamide (DMAc) generates radicals of CH_3 and $CH_2N(CH_3)$

* Corresponding author.
E-mail address: daria-camilla.boffito@polyml.ca (D.C. Boffito).

[1] Given her role as Executive Editor of this journal, Daria Camilla Boffito had no involvement in the peer-review of articles for which he was an author and had no access to information regarding their peer-review. Full responsibility for the peer-review process for this article was delegated to another Editor.

https://doi.org/10.1016/j.ultsonch.2025.107418
Received 7 October 2024; Received in revised form 21 May 2025; Accepted 2 June 2025
Available online 4 June 2025

Nomenclature

b	Radius of the cone in the whistle area
c	Speed of sound
C	Constant
CI	Confidence interval
d	Damping factor
D	Thermal diffusivity of gas
DMAc	N,N-Dimethylacetamide
f	Ultrasonic frequency
h	Gap between the reflector and transducers
HIFU	High intensity focused ultrasound
i	Imaginary unit
IL	Ionic liquid
k_m	Complex wave number
LiCl	Lithium chloride
n_b	Bubble number density
P	Effective acoustic power
p	Acoustic pressure
p_a	Pressure amplitude
p_{atm}	Atmospheric pressure
p_c	Pressure threshold for cavitation
p_{HIFU}	HIFU transducer acoustic pressure
p_{LT}	Lateral transducer acoustic pressure
p_T	Total acoustic pressure[2]
p-Tos	P-toluenesulfonyl chloride
p_v	Vapour pressure
p_0	Static pressure
PI	Process intensification
R_{eq}	Equilibrium radius of bubbles
R_0	Incipient radius of a monodispersed bubble
S	Transducer surface area
t	Time
US	Ultrasound
V	Active cavitation surface area

Greek letters

α	Acoustic attenuation from the liquid
β	Bubbles volume fraction
γ	Specific heat ratio
μ	Dynamic viscosity
ρ	Density
Σ	Surface tension
Φ	Complex adimensional parameter
χ	Adimensional parameter
ω	Acoustic wave angular frequency
ω_0	Bubbles resonant frequency

[2] Sum of the scattered pressure and the background pressure wave.

$C(O)CH_3$ [11]. Collins et al. [12] sonicated DMAc at 490 kHz and 50 W, which generated 3.8 μg mol^{-1} min^{-1} of radicals. US finds application in many reactions: esterification [13], transesterification [14], emulsification [15], carboxymethylation [16], delignification [17] and others. One can tune the energy delivered by US to the reaction to selectively cleave specific bonds [4].

Acoustic cavitation depends on the reaction parameters and on the reactor's geometry [2]. Numerical simulation is a powerful tool to predict, map, and estimate the extent of the acoustic activity during the design or scale-up of sonoreactors. Rashwan et al. [18] numerically investigated the effect of the US frequency, power and probe immersion depth on the acoustic pressure of the fluid. They concluded that higher US frequency favors higher pressure amplitude, with a maximum of negative pressure of -80×10^5 Pa and -70×10^5 Pa in the range of 60 kHz to 80 kHz. Additionally, they found that the probe immersion depth does not impact the acoustic pressure amplitude [18]. On the contrary, Garcia-Vargas et al. [19] suggested that the sonochemical yield significantly changes when varying the probe immersion depth at constant input power and constant liquid volume. Girard et al. [20] varied the size of the reactor, the probe immersion depth and axial position for the dispersion of nanocellulose. An off-centered configuration of a horn-type probe in a small beaker (60 mL) was the most energy-efficient set-up – it decreased the dead zone volume ratio by 61 % and increased the dispersity index by 27 %. Laajimi et al. [21] evaluated the effect of US frequency, probe immersion depth and reactor's diameter on the yield of biolubricant synthesized from canola oil and poly-alcohols. They solved the reaction rate numerically in order to calculate the molar concentration of biolubricant. The fluid velocity and the lubricant yield were the highest with a probe immersion depth of 3 cm in 6 cm of liquid: 1.42 m s^{-1} and 94 %, respectively, versus 1.38 m s^{-1} and 81 % at 1 cm immersion depth. They attributed these results to the shorter distance between the probe tip and the reactor walls, which promotes sound waves reflection and decreases sound attenuation. Moreover, a US frequency of 100 kHz produced 99 % yield compared to 94 % at 20 kHz, with a difference lower than 10 % between the numerical and experimental results [21]. Similarly, Son et al. [22] investigated the sonochemical oxidation activity through KI dosimetry for various reactor geometries in a 20 kHz US system. The highest triiodide concentration developed with a centered probe at an immersion depth of 6 cm, justifying the highest cavitation activity. They attributed this to the reflections of sound waves at the bottom of the reactor and at the liquid surface. They also observed that the off-centered probe affected negatively the mixing pattern of the fluid and decreased the cavitation activity by 30 % [22]. Fang et al. [23] numerically and experimentally investigated the effect of the shape of the probe tip (flat, truncated and conical) on the acoustic streaming and cavitation activity. The sonochemical activity and the average streaming velocity of the conical tip was ~ 67 % higher and 139 % than that of the flat tip. However, the average streaming velocity measured at a distance of 70 mm to 80 mm from the tip, was 1.6 times higher for the flat tip than for the conical one [23].

Continuous US reactors with multiple lateral transducers are versatile as they offer the option for the transducers to emit at different frequencies and promote the constructive interference of sound waves, ensuring a more uniform cavitational activity [2]. Gogate et al. [24] compared the performance of a hexagonal reactor with six lateral transducers to a US bath of 750 mL (22 kHz and 120 W rated output power) and a US probe (22.7 kHz and 240 W rated power dissipation) inserted in a 50 mL reactor. The hexagonal reactor operates at seven different frequency combinations, with a total power dissipation of 900 W and a volume of 7 L. With all transducers emitting at 20 kHz, the cavitation yield in the hexagonal reactor was two times higher than that

Table 1
Values for the pressure threshold for cavitation (p_c).

f, kHz	p_c, Pa
38—82	1.02×10^5
390	1.04×10^5

in the US bath, and 20 times higher than with the US probe [24]. Manickam et al. [25] synthesized biodiesel in a hexagonal multiple frequency reactor. The yield for a triple frequency operating configuration (28 kHz − 40 kHz −70 kHz) was 8 % higher than that of a single frequency (28 kHz), and 3.5 % higher for the double frequency configuration (40 kHz −70 kHz). Prabhu et al. [26] numerically quantified the cavitation activity in the same reactor reported by Gogate et al. [24]. They concluded that the three frequencies configuration created cavitation bubbles 100 % and 30 % larger than the two frequencies and single frequency configurations. Kumar et al. [27] experimented a hexagonal sonoreactor (radius of 0.060 m and length of 0.30 m) with a central tube and three transducers on each side. They measured the maximum acoustic pressure at 0.18 m from the bottom of the reactor, which they attributed to the influence of every transducer. The acoustic pressure decreased from the side to the center of the reactor: from 2.7×10^5 Pa to 2.0×10^5 Pa at 50 kHz. They confirmed that the acoustic pressure is more uniform than using an immersion probe: 10 % to 30 % of variation in their reactor, against 100 % to 400 % for an immersion probe. They explained it by the higher number of transducers and overlapping of waves of every transducer [27]. In an US bath with five transducers at 37 kHz, the acoustic pressure decreased by a factor of 3 at 100 mm of the transducers [28]. Gogate et al. [29] wrote that hexagonal or rectangular cross-section reactors form standing waves which increase the cavitational intensity. Transducers mounted on opposite parallel walls of the reactor generate standing waves via constructive interference, which does not occur in reactors with an odd number of walls [29]. Hodnett et al. [30] measured the maximum acoustic pressure in a cylindrical sonoreactor equipped with ten rows of three transducers equally distributed around the reactor. The maximum acoustic pressure was at the center of the reactor. They observed a similar pressure amplitude close to the reactor wall at 500 W and 25 kHz. It induced cavitation close to the walls, which prevented cavitation from occurring towards the center of the reactor due to acoustic pressure attenuation [30]. Chu et al. [31] simulated a hexagonal three-frequency sonoreactor, with each face-to-face transducer at the same frequency (28 kHz, 40 kHz and 70 kHz). Among the three frequencies, 40 kHz had highest absolute pressure amplitudes, which they confirmed by analyzing each frequency separately and by varying the length of hexagon edge. The absolute pressure decreased by 18 % when increasing the length of the hexagon edge by 50 %, which they attributed to attenuation. Each frequency corresponds to a different wavelength, and they selected the reactor size to ensure that sound waves at 40 kHz produced optimal constructive interference [31].

In this work, we developed a model to quantify the acoustic pressure distribution and the surface area of the active cavitation zones[3] in a continuous cylindrical ultrasonic reactor with six lateral flat transducers along the walls and a concentric high intensity focused ultrasound (HIFU) transducer at the bottom of the reactor. The model accounts for the presence of cavitation bubbles and their effect on sound attenuation. We fixed the US frequency and investigated the influence of the size of the gap between the reflector and the transducers, and the dimension of the whistle on the acoustic cavitation throughout the US reactor. Simulations were conducted in COMSOL Multiphysics. For the first time, we measured experimentally the speed of sound in cellulose esters reaction mixtures, as these were gaps in the literature. These media are part of a bigger biomass conversion project in our research group.

2. Mathematical model and governing equations

2.1. Equations for acoustic pressure

The Helmholtz equation is a steady state form of the wave equation (the latter characterizes the acoustic pressure distribution in time and space). We assumed that the fluid is homogenous – i.e. bubbles are homogeneously dispersed in the fluid – and incompressible (Section 2.3), the sound waves are linear, and the shear stress is negligible [18]. We also assumed that acoustic pressure has a harmonic time dependence: $p(r,t) = p(r).e^{i\omega t}$ [32], where $\omega = 2\pi f$ is the wave's angular frequency in rad s^{-1}, where f is the ultrasonic frequency in Hz. We solved the Helmholtz equation (Eq. (1)) for the acoustic pressure distribution in a liquid:

$$\frac{1}{\rho}\nabla^2 p + \frac{\omega^2}{\rho c^2} p = 0 \tag{1}$$

US applied to a liquid at a certain intensity and frequency generates acoustic cavitation. Bubbles form and accumulate at the tip of the US probe and attenuate the propagation of sound waves. The modified Helmholtz equation includes the damping effect of bubbles, arising from viscous, thermal and acoustic effects (factor d defined later). This model does not consider the ultrasound probe tip as a moving wall as it should. The~~ir~~ modified Helmholtz equation (Eq. (2)) is:

$$\nabla^2 p + k_m^2 p = 0 \tag{2}$$

where k_m is the complex wave number in m^{-1} in the fluid and bubbles mixture. For a monodisperse bubble distribution, k_m^2 is [33]:

$$k_m^2 = \frac{\omega^2}{c^2}\left(1 + \frac{4\pi c^2 n_b R_0}{\omega_0^2 - \omega^2 + 2id\omega}\right) \tag{3}$$

where n_b is the number of bubbles per unit volume in m^{-3}, R_0 is the incipient radius of a bubble in m, ω_0 is the resonant angular frequency of bubbles in rad s^{-1}, i is imaginary unit and d is the damping factor (a term for the viscous, thermal and acoustic effects respectively [34]) determined from Eq. (4):

$$d = \frac{2\mu}{\rho R_{eq}^2} + \frac{p_0}{2\rho\omega R_{eq}^2} Im\Phi + \frac{\omega^2 R_{eq}}{2c} \tag{4}$$

where p_0 is the undisturbed pressure in the bubble position in Pa, which is $p_{atm} + (2\sigma/R_{eq})$ where σ is the surface tension of the liquid in N m^{-1}. R_{eq} is the bubbles equilibrium radius in m and it accounts for direct contact coalescence and rectified diffusion, μ is the dynamic viscosity of the fluid in Pa s, and Φ is a complex adimensional parameter. The resonant angular frequency of bubbles ω_0 in Eq. (3) corresponds to:

$$\omega_0^2 = \frac{p_0}{\rho R_{eq}^2}\left(Re\Phi - \frac{2\sigma}{p_0 R_{eq}}\right) \tag{5}$$

The parameter Φ in Eq. (4) and in Eq. (5) is a function of the specific heat ratio of the gas inside bubbles (γ), and χ (Eq. (7) [35], Eq. (6) determines it:

$$\Phi = \frac{3\gamma}{1 - 3(\gamma - 1)i\chi[(i/\chi)^{1/2}\coth(i/\chi)^{1/2} - 1]} \tag{6}$$

χ is expressed as:

$$\chi = D/\omega R_{eq}^2 \tag{7}$$

with D the thermal diffusivity of the gas. The bubbles number density n_b in Eq. (3) depends on β, the volume of the gas fraction within the bubbles in the reactor with respect to the total volume:

$$n_b = \frac{3\beta}{4\pi R_0^3} \tag{8}$$

Other authors adopted the same theoretical approach [23,33,36] and validated it experimentally, either by: particle image velocimetry [23] or through sonochemiluminescence [36].

[3] Area in which the pressure is above the Blake pressure threshold, where cavitation is considered active.

2.2. Equations for acoustic cavitation zones

We considered that bubbles grow and eventually collapse and generate cavitation when the pressure is above the threshold pressure for cavitation, p_c [37]. This pressure threshold depends on the sonicated fluid, its temperature and its gas content, and is expressed by Eq. (9):

$$p_c = p_0 - p_v + \frac{\frac{2}{3\sqrt{3}}\sqrt[3]{\left(\frac{2\sigma}{R_{eq}}\right)^2}}{\sqrt{p_0 - p_v + \frac{2\sigma}{R_{eq}}}} \tag{9}$$

where p_0 is the vapour pressure of the sonicated liquid in Pa.

2.3. Assumptions of the model

For Eq. (1) and Eq. (2), we assumed:

1. The fluid is incompressible and Newtonian. The reactor intends to treat aqueous solutions of lignin, and solutions of cellulose esters in dimethylacetamide (DMAc) and lithium chloride (LiCl). The compressibility of DMAc – 6.7×10^{-4} MPa^{-1} [38] – is comparable to that of water – 4.6×10^{-4} MPa^{-1} [39]. LiCl is an electrolyte, causing electrostriction and reducing compressibility. Wahab and Mahiuddin [40] demonstrated that increasing the concentration of LiCl in methanol decreased the compressibility of the mixture. Given that methanol is an organic solvent, we assume a similar behavior for the DMAc/LiCl system.
2. The bubble to liquid volume ratio is low so the medium's properties are those of the liquid phase [34].
3. The thermodynamic properties of the liquid medium are independent of the temperature and bubble volume fraction.
4. We set the bubble size R_0 equal to 1.6 µm at a US frequency of 40 kHz and to 0.1 µm at a US frequency of 390 kHz. Brotchie et al. [41] and Dehane et al. [42] observed that an increase of the acoustic frequency, decreased the mean size of the cavitation bubbles, and an increase of the acoustic power, increased the mean size of the cavitation bubbles. Servant et al. [43] and Dähnke et al. [44] assumed the bubble radius ranged between 5×10^{-6} m and 3×10^{-3} m. Pandit et al. [45] chose a bubble radius ranging from 2 µm to 50 µm with the acoustic frequency ranging from 10 kHz to 80 kHz. We chose a bubble equilibrium radius of 80 µm at a US frequency of 40 kHz and of 5 µm at a US frequency of 390 kHz. It respects the order of magnitude of the Minnaert's equation: $R_{eq} \approx 3/f$ [41]. Under acoustic activity and coalescence, cavitation bubbles grow to about 50 times R_0 [46].
5. The distribution of bubbles is homogeneous in the reactor and β ranges from 10^{-4} to 10^{-1}. For values $\beta > 10^{-1}$ bubbles scatter most of the sound waves [33]. For the computation, similarly to Dähnke et al. [44], we assumed that the volume fraction of bubbles in the reactor linearly depends on the acoustic pressure amplitude in the fluid: $\beta =$

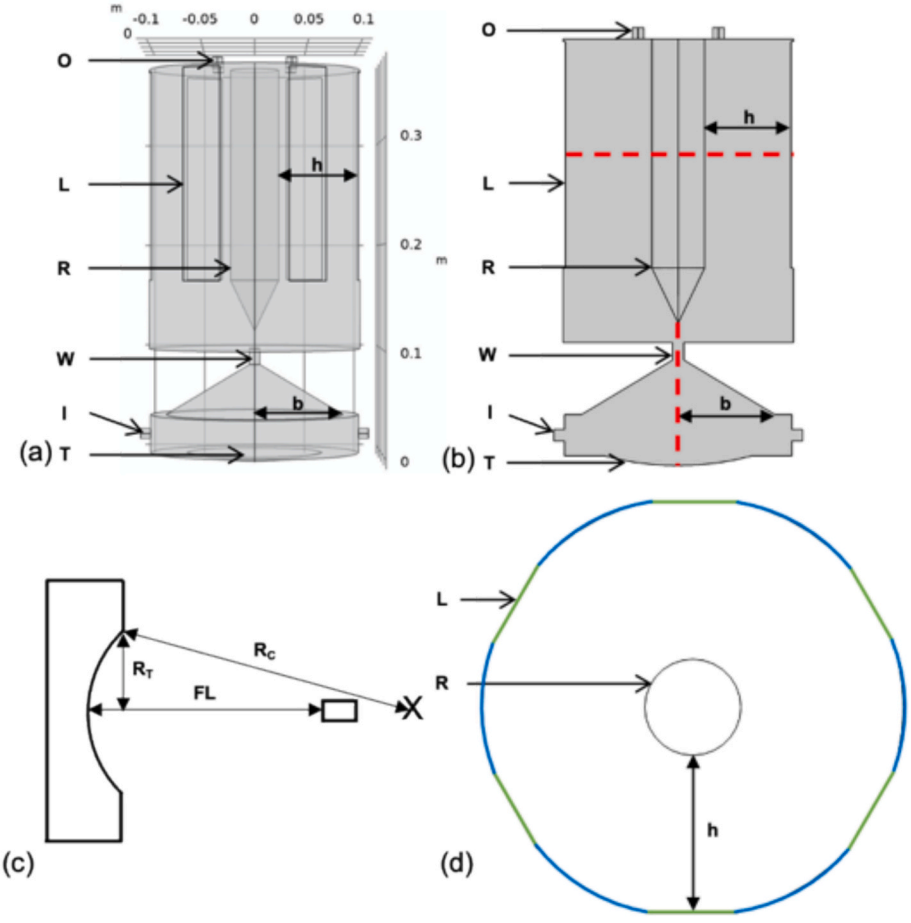

Fig. 1. Sonochemical reactor (a). Longitudinal section (b), red dashed lines are the mesh sensitivity study measurement segments. HIFU transducer scheme (c). Cross section (d), green lines are the lateral transducers and blue arcs are the reactor's wall. h is the gap between the lateral transducers and the reflector. b is the radius of the cone in the whistle area. O and I correspond to the fluid outlets and inlets, respectively. L and T correspond to the lateral and HIFU transducers, respectively. R and W correspond to the reflector and whistle parts, respectively. FL is the focal length, R_C is the curvature radius and R_T is the radius of the transducer.

C·p where C is a constant. Jamshidi et al. [33] validated this model in water, with $C = 2 \times 10^{-9}$. We chose the same value for C.

6. The US transducers generate acoustic pressure amplitude, which is the greatest in the middle of the transducers face and decreases as the distance from the center increases [37]. The decrease in pressure amplitude follows a Gaussian function.
7. The assumption of a linear propagation of acoustic waves is valid for: $p \ll \rho \cdot c^2$. This assumption holds for values of approximately 2×10^7 Pa for our fluids [47]. It also holds as the propagation media is homogeneous [48]. The nonlinearity of waves propagation has more pronounced effects above 100 W cm^{-2} at 1 MHz [49]. Simulations of HIFU transducers with linear propagation assumption was successful and verified experimentally [50].

3. Simulation

3.1. Geometry and boundary conditions

The reactor is a 12 L stainless steel two-piece vessel (Fig. 1a and b). The upper part consists of a cylinder (ID: 0.2 m, OD: 0.22 m) with six Ti64 (Ti-6Al-4 V alloy) US transducers along its walls (200 mm x 40 mm), and a stainless steel cylindric reflector in the middle (D: variable, H: 0.02 m). The lower part consists of a cylinder (ID: 0.2 m, OD: 0.22 m, H: 0.0365 m) that houses a concentric high intensity focus US transducer (Ti64, 0.125 m curvature radius, 0.065 m radius (Fig. 1c), and a conic whistle that streamlines the flow towards the upper part of the reactor. The reactor has two liquid feed inlets (I, Fig. 1a) located at the bottom of the reactor, and four outlets located at very top of the reactor (O, Fig. 1a). The transducer material and mounting are proprietary information, part of a patent pending and not published yet.

The difference of impedance Z (product of material's density and speed of sound) at interfaces induces ultrasound reflection. We set the following boundary conditions for the simulations:

- At the reactor's walls, the impedance was: $Z = 8010$ kg m^{-3} * 3070 m s^{-1} (for stainless steel 304L).
- At the boundary fluid-transducer (non-active), the impedance was: $Z = 4470$ kg m^{-3} * 4987 m s^{-1}.
- We defined a pressure amplitude p_a (Eq. (10)) at the surface of the US transducers:

$$p_a = \sqrt{\frac{2Pc\rho}{S}} \tag{10}$$

where P is the US power delivered to the liquid, and S is the ultrasound transducer surface area.

3.2. Mesh

COMSOL Multiphysics generated the mesh automatically with triangle elements (268 566 elements) for the 2D geometry. A mesh size sensitivity study verified the convergence of the model among three extremely fine mesh element sizes: maximum size of 0.0075 cm and minimum size of 0.00075 cm; maximum size of 0.075 cm and minimum size of 0.00075 cm; maximum size of 0.40 cm and minimum size of 0.00079 cm. Moreover, we ensured the maximum mesh element size was 1/5 of the US wavelength (at 390 kHz, $\lambda = 0.38$ cm, maximum size of 0.075 cm and minimum size of 0.00075 cm) [20]. Even though other sources suggest at least 8 mesh elements per wavelength [18]. The software calculated the acoustic pressure along the segment located at half of the reflector's length (100 mm, Fig. 1b) and the segment in the axis of the HIFU transducer (Fig. 1b).

We applied a quadratic Lagrange discretization to solve the model, which provides more accuracy with fewer elements per wavelength. It better represents the curved geometry. We chose the MUMPS (MUltifrontal Massively Parallel sparse direct Solver) solver as it uses less memory than the PARDISO solver. The Newton method improves the convergence of the solver. We kept an initial damping factor of 1 as the model converged. The maximum number of iterations was 25, which is sufficient to reach convergence for our model in a reasonable time.

3.3. Simulation steps

COMSOL Multiphysics 5.5 solved the equations in Section 2 and calculated the acoustic pressure distribution throughout the sonoreactor, with and without bubbles attenuation. The software solved the equations in 2D for computation time saving.

The simulation followed two steps for the lateral transducers and for the HIFU transducer:

1 The COMSOL acoustic module – Pressure Acoustics solved Eq. (1) in the frequency Domain, modelling a continuous wave and considering the attenuation of the acoustic pressure (α, Eq. (11)) intrinsic to the medium [18]. The study calculates the acoustic pressure distribution without cavitation bubbles, which is the starting point for step 2

$$\alpha = \frac{8\mu\pi^2 f^2}{3\rho c^3} \tag{11}$$

2 We included the attenuation due to cavitation bubbles by implementing Eq. (2) in the Stabilized Convection-Diffusion equation and defining Eq. (3) to Eq. (8) into the parameters. The software calculated β with the acoustic pressure determined in step 1. Then, it solved Eq. (8) and Eq. (3) to determine n_b and k_m, and it finally solved the modified Helmholtz equation Eq. (2) until steady state

Because the lateral transducers and the HIFU operate at different frequencies, COMSOL Multiphysics resolved Step 1 and Step 2 for the two transducers individually, thereby mapping the acoustic pressure as if the lateral transducers and the HIFU operated one at a time. The total acoustic pressure field (p_T) across the reactor was calculated through the superposition principle using the Parseval's theorem (Eq. (12)) [31]. This is possible because the power and frequency chose for this work allow for the simulation of propagating waves as linear, (assumption 7 in Section 2.3). [38]:

$$p_T = \sqrt{\frac{1}{2}\left(|p_{LT}|^2 + |p_{HIFU}|^2\right)} \tag{12}$$

where $|p_{LT}|$ and $|p_{HIFU}|$ are the module of acoustic pressure generated by the lateral transducers and HIFU transducer, respectively.

4. Material and methods

4.1. Simulations operating parameters and design of experiments

Each lateral transducer emits at 400 W of electrical power and 340 W of nominal power. We assumed that the transducers converted 85 % of the electrical power into acoustic power. The HIFU transducer emits at 120 W of electrical power, thus its power intensity supports the linear propagation [49]. The HIFU transducer emits at 390 kHz. At frequencies of a few hundreds kHz, cavitation generates mostly chemical effects like radicals generation [2]. The lateral transducers and the HIFU transducer were active separately first, in order to determine the total acoustic pressure and active cavitation surface area. We built two designs of experiments (DOE).

DOE 1 investigated the effect of the geometry (h and b) and frequency (f) on the total acoustic pressure (p_T) and active cavitation surface area (V) within the sonoreactor. The input variables and their associated levels are:

Table 2
Input variables for DOE 1 and DOE 2, with their levels.

Input variable	DOE 1 f, kHz	h, m	b, m	DOE 2 f, kHz	Cellulose concentration, g L^{-1}
Levels	38	0.075	0.05	38	6.25
	40	0.077	0.075	40	12.5
	42		0.1	78	25.0
	78			80	
	80				
	82				

- the ultrasound generator frequency, six levels (Table 2). With US frequencies from 20 kHz to 100 kHz, cavitation generates mainly physical effects, like liquid circulation and turbulence, and chemical effects in a lower extent [16].
- the gap between the lateral transducers and the reflector (h), two levels (Table 2). We designed the gap between the transducers and the reflector to be a multiple of the wavelength to ensure constructive interference of the waves. We accounted for frequency variations resulting from the probe wearing over time.
- the radius of the cone in the whistle area (b) (Table 2).

DOE 2 investigated the effect of the cellulose solutions' parameters on the total acoustic pressure and cavitation surface volume within the sonoreactor (fixed geometry). $h = 0.075$ m and $b = 0.1$ m yielded the largest cavitation surface volume in DOE 1, hence DOE 2 adopted these fixed geometric values. The input variables for DOE 2 and their associated levels are:

- The viscosity (μ), density (ρ) and speed of sound (c) of three concentrations of cellulose solution, 3 levels (Table 2).
- the frequency, four levels (Table 2).

We conducted a statistical analysis, in JMP statistical software, to identify significant dependent variables and relationship within the data, and to fit linear models [36]. We first ran a predictor screening analysis with Bootstrap forest partitioning, which identified the dependent variables responsible for the largest variance for the response variables p_T and V. The software generates random forest algorithm to evaluate the contribution of each predictor (input variable) to the response variable. Hundred decision trees are built with bootstrap of the data, thus input variables are ranked from the most significant to the least significant. We then eliminated the non-significant variables to fit a linear regression model.

4.2. Liquid media: Preparation and characterization

The objective of the simulations was to calculate the acoustic pressure in cellulose esters in N,N-dimethylacetamide (DMAc). The choice of these media was dictated by ongoing investigations in our research group as a part of a bigger project.

We measured the density and the viscosity at 20 °C, after 2 h of cellulose esterification at 3 different concentrations (25 g L^{-1}, 12.5 g L^{-1} and 6.25 g L^{-1}). An oven dried cellulose at 100 °C for 1 h prior to processing. A solution of 20 mL of DMAc activated 0.50 g of cellulose (or 0.25 g, or 0.125 g depending on the concentration) at 130 °C for 2 h under stirring at 300 rpm. The mixture cooled to 100 °C and we added 1.5 g of lithium chloride (LiCl), to enhance cellulose dissolution and electrostriction [51,52]. Stirring continued with the heating turned off until the mixture reached room temperature and was completely transparent. We added 3.53 g of p-toluenesulfonyl chloride (p-Tos) as activating agent [52], and 5.26 g of oleic acid, which were *a priori* dissolved in 5 mL of DMAc. Regardless of the cellulose concentration, the molar ratio cellulose: oleic acid: p-Tos remained constant at 1: 6: 6. The esterification reaction took place in a thermostatic beaker at 20 °C and 300 rpm for 2 h.

An Anton Paar DMA 4500 density meter determined the density of the cellulose esters' solutions at 20 °C, after reaction. Similarly, a Thermo Scientific Haake Viscotester iQ with a 3 mL coaxial chamber assessed the viscosity of the cellulose solutions after reaction. First, there was a ramp for 120 s at a shear rate of 1 s^{-1}, followed by an increase in the shear rate to 500 s^{-1} in 10 steps over 10 min. COMSOL Multiphysics employed the values we measured (Table 3) for the numerical simulations.

4.3. Speed of sound measurements

An Olympus V306 immersion transducer determined the speed of sound of cellulose esters solutions. The transducer active element has a diameter of 13 mm and the total diameter of the transducer is 16 mm. The transducer operates at 2.25 MHz and transmits the signal through a polystyrene container filled with 50 mL of the solution. The transducer adhered to the side of the container and we fed the solution with a pipette to prevent movement during the filling and emptying the container, ensuring that the waves transmit perpendicularly to the opposite side of the container. We connected the transducer to an Agilent Technologies 33220A 20 MHz Waveform Generator (signal generator) and to a GW Instek GDS-1000A-U Series oscilloscope.

First, we transmitted a signal through deionized water to measure the round-trip distance the sound wave travelled through the fluid. We assumed the sound wave travelled only in water, at a speed of 1498 m s^{-1}, as measuring the thickness of the gel and the polystyrene wall was impossible. The round-trip travel time corresponds to the interval between the start of each peak (red lines in Fig. 2). The sound wave travelled a total distance of 0.04467 m. The oscilloscope measured the speed of sound seven times and calculated a mean value. We entered these values into COMSOL Multiphysics for simulations (Table 3).

Assuming that the wave traveled only through the fluid led to an underestimation of the speed of sound. In reality, the speed of sound in polystyrene is twice as high in water, oils, and ethanol, for example [53]. Consequently, we overestimated the sound attenuation in the solutions.

5. Model validation

As the reactor was unavailable for experimental validation due to unfinished commissioning, we validated the model through a benchmarking approach. This approach consists in comparing the results of our simulation code with established sources of validated data [27]. We applied our model equations to the published geometry of Kumar et al. [27], using their fluid and US parameters. We compared the simulated acoustic pressure to what they obtained along the radial axis of the reactor. They measured the pressure into the hexagonal reactor with a hydrophone placed at different radial and axial positions [27].

The reactor is a 7.5 L hexagonal vessel (height of 0.3 m and length of side wall of 0.1 m), with three circular US transducers (diameter of 0.06 m, spaced 0.03 m apart, each operating at 50 W and 50 kHz) along each wall. The vessel is filled with water [27].

The acoustic pressure had the same order of magnitude as the local pressure measured by Kumar et al. However, the pressure profiles differed (Fig. 3). At a radial position of 0.015 m, the pressure of this model was 38 % lower than the measured pressure at 0.005 m away from the bottom of the reactor, whereas it was only 1 % lower at 0.14 m

Table 3
Properties of cellulose esters solutions.

Cellulose concentration, g L^{-1}	Speed of sound, m s^{-1}	Density, kg m^{-3}	Viscosity, Pa. s
25	1495.8	936.2	23.3×10^{-3}
12.5	1529.6	939.1	14.1×10^{-3}
6.25	1545.0	941.8	5.3×10^{-3}

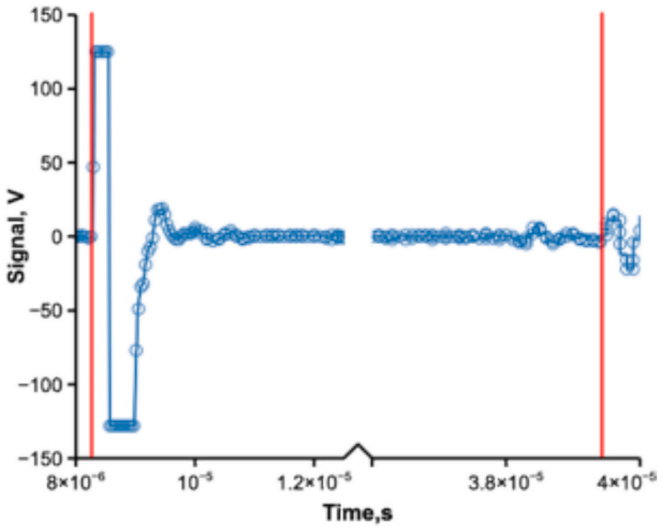

Fig. 2. Results of the signal in deionized water. Red vertical lines correspond to the signal inbound and outbound.

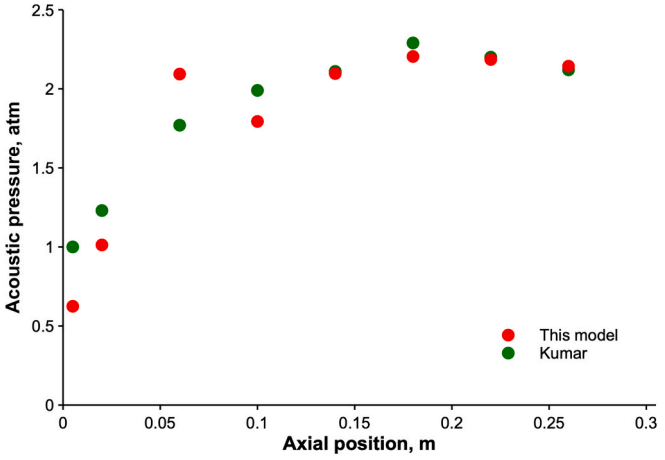

Fig. 3. Absolute acoustic pressure along the axial position at a radial position 0.015 m, and the comparison with the mean local pressure of Kumar et al. at the radial position 0.015 m [27].

and 0.22 m away from the bottom of the reactor (Fig. 3). This difference arises from Kumar et al. measuring the local mean pressure, which is time-averaged. In our simulation, COMSOL Multiphysics calculated the absolute value of the instantaneous local acoustic pressure in a stationary phase. Other sources of error include the simulation not accounting for interactions of acoustic waves, or nonlinear acoustic phenomena. Although direct experimental validation remains the preferred approach, benchmarking validation confirms that the acoustic pressure simulated in our model aligns in order of magnitude and similarity with values reported in the literature. This demonstrates that our model is reliable.

6. Results and discussion

6.1. Effect of the frequency

p_T increases with the increase of f and decreases as h increases. V increases as f increases and decreases as h increases (Fig. S1). b does not have a significant effect on p_T and V, accounting for 5.1 % and 8.1 % of the variance respectively (Table 4). Thus, we selected f and h and neglected b for the linear regressions with a one-degree interaction.

Table 4
Predictor screening analysis of p_T and V for DOE 1. *Portion of the variance explained by the predictor for p_T and V. **p-value of the density ellipse of 0.95 for p_T and V. A p-value above 0.05 means the data are not sufficiently significant to refute the assumption of random distribution within the ellipse. Whereas a p-value below 0.05 suggests the data points are not randomly distributed.

	Predictor		Bivariate fit	
Input variables	p_T*	V*	p_T**	V**
f	60.6 %	57.7 %	0.13 > 0.05	0.76 > 0.05
h	34.3 %	34.1 %	0.04 < 0.05	0.08 > 0.05
b	5.1 %	8.1 %	0.98 > 0.05	0.96 > 0.05

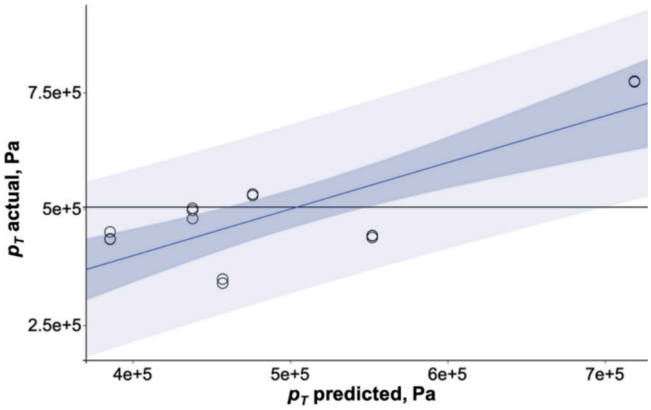

Fig. 4. Actual by predicted p_T (○) for frequencies from 38 kHz to 42 kHz. Regression, 95 % CI of prediction, RMSE = 88699, R^2 = 0.655, p-value = 0.0015, Mean of response (504582 Pa), Prediction interval.

The statistical analysis generated the following regression equation for p_T from 38 kHz to 42 kHz (Fig. 4):

$$p_T = 6.0 \times 10^6 - 4.6 \times 10^4 \bullet f - 4.8 \times 10^7 \bullet h + 36.9 \times 10^6 \bullet (f - 40)(h - 0.076) \quad (13)$$

The statistical analysis generated the following regression equation for p_T from 78 kHz to 82 kHz (Fig. 5):

$$p_T = 32.3 \times 10^6 - 1.7 \times 10^5 \bullet f - 23.3 \times 10^7 \bullet h + 20.2 \times 10^7 \bullet (f - 80)(h - 0.076) \quad (14)$$

p_T increases with the increase of frequency. However, for $h = 0.075$ m, from 38 kHz to 42 kHz, p_T decreases (Eq. (13)) by 44 %, and from 78 kHz

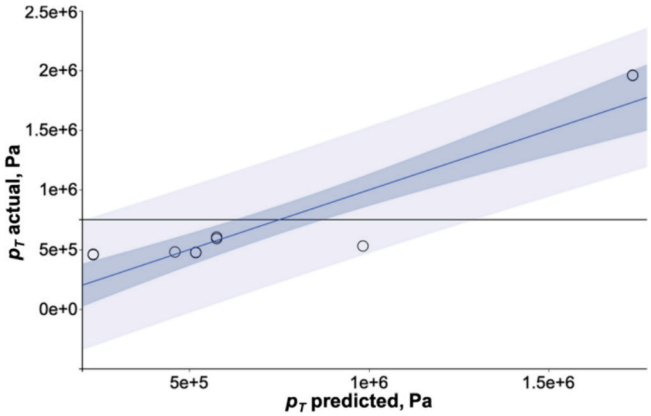

Fig. 5. Actual by predicted p_T (○) for frequencies from 78 kHz to 82 kHz. Regression, 95 % CI of prediction, RMSE = 257947, R^2 = 0.820, p-value < 0.0001, Mean of response (750281 Pa), Prediction interval.

to 82 kHz it decreases (Eq. (14)) by 77 %, with a maximum of 1.96×10^6 Pa at 78 kHz. For $h = 0.077$ m, from 38 kHz to 42 kHz, p_T decreases by 10 %, and from 78 kHz to 82 kHz it increases by 26 %. The increase of amplitude of acoustic pressure with f was also observed by Rashwan et al. [18]. When the frequency increases, the collapse of cavities is more violent and the power dissipation increases, which increases p_T [27]. Leighton explained that a higher f results in lower wavelength focusing more energy in space, resulting in increased p_T [8].

The statistical analysis generated the following regression equation for V from 38 kHz to 42 kHz (Fig. 6):

$$V = 0.036 + 3.9 \times 10^{-4} \bullet f - 0.27 \bullet h + 1.5 \bullet (f - 40)(h - 0.076) \quad (15)$$

The statistical analysis generated the following regression equation for V from 78 kHz to 82 kHz (Fig. 7):

$$V = 0.20 - 21.6 \times 10^{-4} \bullet f - 2.0 \bullet h + 2.4 \bullet (f - 80)(h - 0.076) \quad (16)$$

V increases as the frequency increases and follows the same trends as p_T. For h = 0.075 m, from 38 kHz to 42 kHz, V decreases (Eq. (15)) by 14 %, and from 78 kHz to 82 kHz it decreases (Eq. (16)) by 26 %, with a maximum of 3.99×10^{-2} m^2 at 78 kHz. For h = 0.077 m, from 38 kHz to 42 kHz, V increases by 31 %, and from 78 kHz to 82 kHz it increases by 34 %. When the frequency increases, the collapse of cavities is more violent and the power dissipation increases, which increases p_T and increases V [27]. The increase of V with f can be explained by a larger number of cavitation bubbles generated, and shorter collapse time [21]. This phenomenon explains the increase of yield with f that Laajimi et al. observed [21].

6.2. Effect of the geometrical parameters h and b

p_T decreases as the gap between the reflector and transducers (h) increases (Eq. (13) and Eq. (14)). As h increases from 0.075 m to 0.077 m, p_T decreases by 76 % (at 78 kHz) and by 23 % (at 40 kHz) for instance, with a maximum of 1.96×10^6 Pa at 78 kHz for $h = 0.075$ m and $b = 0.1$ m (Fig. 8).

V decreases as h increases (Eq. (15) and Eq. (16)) and follows the same trend observed for p_T. As h increases from 0.075 m to 0.077 m, V decreases by 34 % (at 78 kHz) and by 6 % (at 40 kHz) for instance, with a maximum of 3.99×10^{-2} m^2 at 78 kHz for h = 0.075 m and b = 0.1 m (Fig. 8 and Fig. S2). When h increases, sound waves travel a longer distance in the fluid, leading to greater sound attenuation, which in turn reduces both p_T and V [31]. Studies of Kumar et al., Gogate et al., Hodnett et al. and Chu et al. [27,29–31] confirm our results analysis, which attest to the importance of considering the geometry together with the frequency wavelength when designing the reactor.

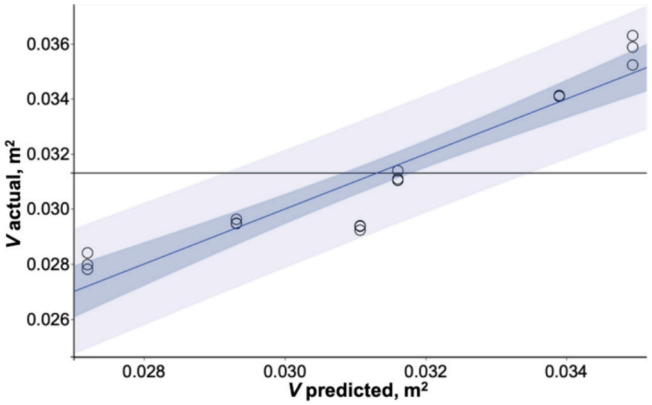

Fig. 6. Actual by predicted V (○) for frequencies from 38 kHz to 42 kHz. Regression, 95 % CI of prediction, RMSE = 0.866, R^2 = 0.889, p-value < 0.0001, Mean of response (0.0313 m^2), Prediction interval.

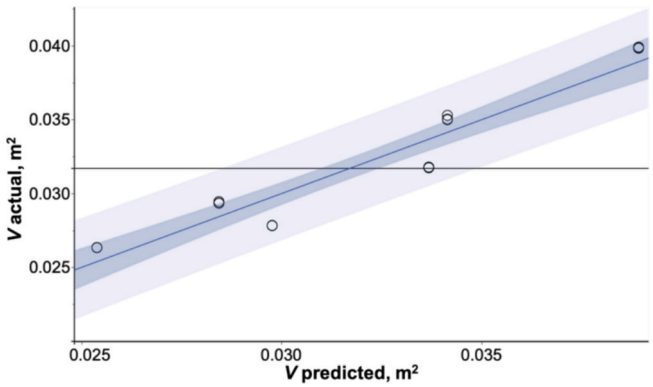

Fig. 7. Actual by predicted V (○) for frequencies from 78 kHz to 82 kHz. Regression, 95 % CI of prediction, RMSE = 0.001, R^2 = 0.913, p-value < 0.0001, Mean of response (0.0317 m^2), Prediction interval.

6.3. Effect of the concentration of cellulose

p_T decreases as μ increases and as ρ decreases. V decreases as μ increases and as ρ decreases. c does not have a significant effect on p_T and V, accounting for 5.2 % and 5.5 % of the variance respectively (Table 5). Thus, we selected μ, ρ and f, and neglected c for the linear regressions with a one-degree interaction.

The statistical analysis generated the following regression (Fig. 9) equation for p_T:

$$p_T = -77.1 \times 10^6 + 8.2 \times 10^4 \bullet \rho + 7.6 \times 10^3 \bullet f - 7.3 \times 10^5 \bullet (f - 59)(\mu - 0.014) \quad (17)$$

p_T decreases as μ increases and as ρ decreases (Eq. (17)). At 78 kHz, when μ increases from 5.3×10^{-3} Pa.s to 23.3×10^{-3} Pa.s, and ρ decreases from 941.8 kg m^{-3} to 936.2 kg m^{-3}, p_T decreases by 75 %. The more viscous the fluid is, the greater the sound attenuation and the lower the resulting acoustic pressure [54]. Denser fluids require more energy to cavitate, thus a larger acoustic pressure.

The statistical analysis generated the following regression (Fig. 10) equation for V:

$$V = 7.5 - 2.9 \bullet \mu - 8.0 \times 10^{-3} \bullet \rho \quad (18)$$

V decreases as the μ increases and as ρ decreases (Eq. (18)). At 78 kHz, when μ increases from 5.3×10^{-3} Pa.s to 23.3×10^{-3} Pa.s, and ρ decreases from 941.8 kg m^{-3} to 936.2 kg m^{-3}, V decreases by 37 %. Less viscous fluids produce more intense shock waves, leading to enhanced cavitation activity and larger V. A higher fluid density requires more energy to induce cavitation, reducing bubbles formation of bubbles and decreasing V. Schieppati et al. explained similar effects of μ and ρ on p_T and V [36].

Although c does not have a significant effect on p_T and V (Table 5), a higher c means that sound waves propagate faster and vibrate more, which increases the acoustic pressure and bubbles collapse, originating larger active cavitation zones. The negligible effect of c may explain why, despite the gap being designed to be twice the wavelength at 40 kHz with a speed of sound of 1495.8 m s^{-1}, the 0.075 m gap did not yield the highest p_T nor the largest V.

7. Conclusions

In this study, we characterized the cavitation activity in a cylindrical ultrasonic reactor with six lateral flat transducers along the walls and a concentric high intensity focused ultrasound transducer at the bottom of the reactor. The hexagonal section reactor design ensures constructive sound waves interference. The HIFU transducer focuses US waves in the conic whistle part, which streamlines the flow towards the upper part of the reactor. COMSOL Multiphysics analyzed the propagation of sound

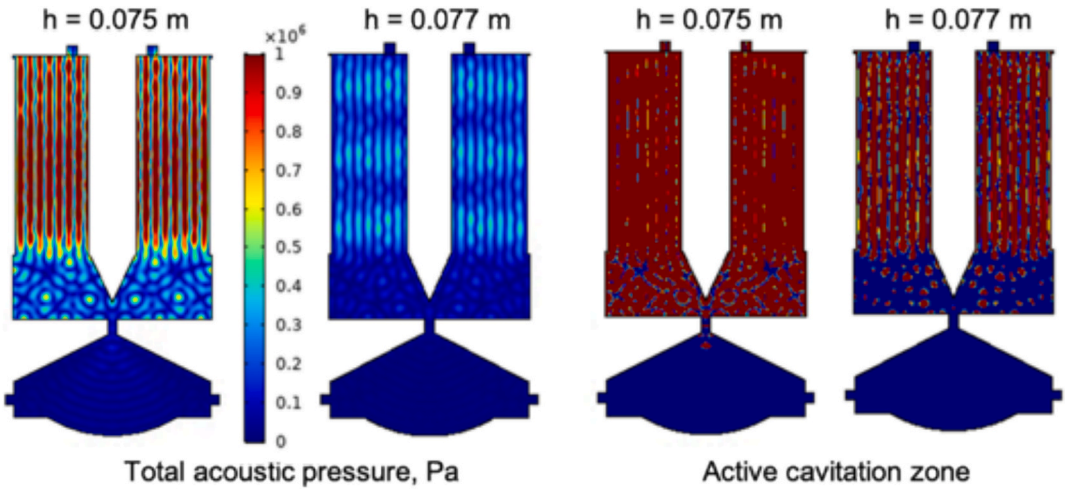

Fig. 8. Total acoustic pressure and active cavitation zones at 78 kHz and b = 0.1 m. Comparison between h = 0.075 m and h = 0.077 m.

Table 5
Predictor screening analysis of p_T and V for DOE 2. *Portion of the variance explained by the predictor for p_T and V. **p-value of the density ellipse of 0.95 for p_T and V. A p-value above 0.05 means the data are not sufficiently significant to refute the assumption of random distribution within the ellipse. Whereas a p-value below 0.05 suggests the data points are not randomly distributed.

	Predictor		Bivariate fit	
Input variables	p_T*	V*	p_T**	V**
f	48.5 %	21.0 %	0.25 > 0.05	0.85 > 0.05
μ	28.6 %	37.1 %	0.14 > 0.05	0.0032 < 0.05
ρ	17.8 %	36.4 %	0.14 > 0.05	0.0032 < 0.05
c	5.2 %	5.5 %	0.17 > 0.05	0.0048 < 0.05

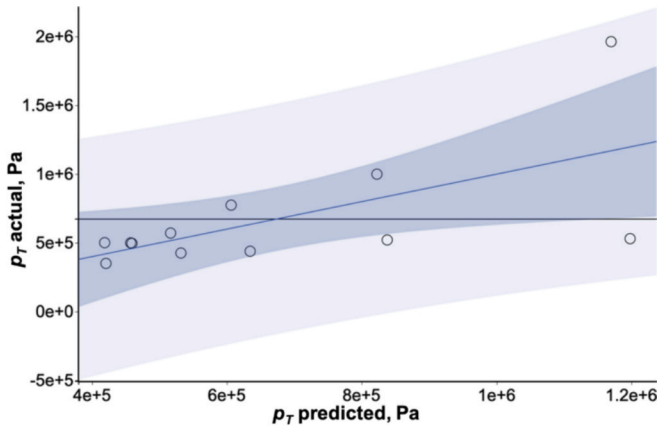

Fig. 9. Actual by predicted plot of p_T (○). Regression, 95 % CI of prediction, RMSE = 403169, R^2 = 0.393, p-value = 0.2383, Mean of response (672635 Pa), Prediction interval.

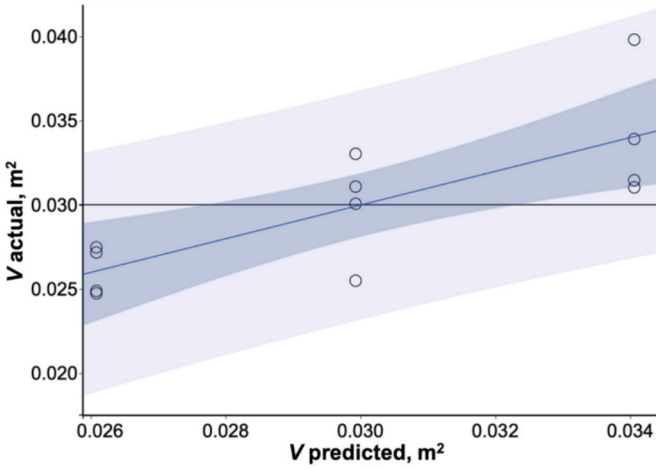

Fig. 10. Actual by predicted plot of V (○). Regression, 95 % CI of prediction, RMSE = 0.003, R^2 = 0.597, p-value = 0.0167, Mean of response (0.0300 m^2), Prediction interval.

waves and the active cavitation zones in the sonoreactor at various geometrical configurations and operating frequencies. At a fixed gap of 0.075 m between the reflector and transducers, the software solved the propagation of sound waves and calculated the cavitation surface area in the sonoreactor for various cellulose concentrations in water and working frequencies. Cavitation bubbles affect the propagation of acoustic waves, thus we included its attenuation in our model. The acoustic pressure was attenuated by 80 %, and the active cavitation surface area by 85 %. Acellulose esters concentration of 6.25 g L^{-1} resulted in the highest p_T and largest V. At 78 kHz and $h = 0.075$ m, with $\mu = 5.3 \times 10^{-3}$ Pa.s and $\rho = 941.8$ kg m^{-3}, the simulation generates $p_T = 1.96 \times 10^6$ Pa and $V = 3.99 \times 10^{-2}$ m^2.

These simulations calculated the activity throughout the entire reactor geometry, coupling the activity of lateral and HIFU transducers. We included the root mean-squared acoustic pressure of two harmonics in the equation $\beta = C \bullet p$. A future work will consider simulations of the HIFU transducer in the nonlinear regime, through simulation in the time domain. This study assumed a constant bubble equilibrium radius. As the pressure increases beyond the Blake threshold, the bubble size distribution widens, leading to nonuniform bubbles. Larger bubbles attenuate sound waves more than smaller ones, thus the present study underestimated sound waves attenuation. To improve the accuracy of the simulation, future works will include a dynamic bubble size distribution model.

CRediT authorship contribution statement

Pierre Dal: Writing – review & editing, Writing – original draft, Validation, Methodology, Investigation, Formal analysis, Data curation, Conceptualization. **Julie Kring:** Project administration, Investogation, Methodology. **Dalma Schieppati:** Writing – review & editing, Validation, Formal analysis, Data curation, Conceptualization, Methodology. **Daria C. Boffito:** Writing – review & editing, Validation, Methodology, Investigation, Formal analysis, Data curation, Conceptualization,

Supervision, Project administration.

Declaration of competing interest

The authors declare that they have no known competing financial interests or personal relationships that could have appeared to influence the work reported in this paper.

Acknowledgements

Pierre Dal is thankful to Institut de l'Energie Trottier for awarding him a graduate scholarship to support his studies. We acknowledge the financial support from Khepra (United States, AL) and of the Natural Sciences and Engineering Research Council of Canada (NSERC). This research was undertaken in part, thanks to funding from the Canada Research Chairs Program.

Appendix A. Supplementary data

Supplementary data to this article can be found online at https://doi.org/10.1016/j.ultsonch.2025.107418

References

[1] D. Fernandez Rivas, D.C. Boffito, J. Faria-Albanese, J. Glassey, N. Afraz, H. Akse, Kamelia V.K. Boodhoo, R. Bos, J. Cantin, Y.W. (Emily) Chiang, J.-M. Commenge, J.-L. Dubois, F. Galli, J.P.G. de Mussy, J. Harmsen, S. Kalra, F.J. Keil, R. Morales-Menendez, F.J. Navarro-Brull, T. Noël, K. Ogden, G.S. Patience, D. Reay, R.M. Santos, A. Smith-Schoettker, A.I. Stankiewicz, H. van den Berg, T. van Gerven, J. van Gestel, M. van der Stelt, M. van de Ven, R.S. Weber, Process intensification education contributes to sustainable development goals. Part 1, Education for Chemical Engineers 32 (2020) 1–14. Doi: 10.1016/j.ece.2020.04.003.

[2] D. Meroni, R. Djellabi, M. Ashokkumar, C.L. Bianchi, D.C. Boffito, Sonoprocessing: from concepts to Large-scale reactors, Chem. Rev. 122 (2022) 3219–3258, https://doi.org/10.1021/acs.chemrev.1c00438.

[3] D.C. Boffito, T. Van Gerven, Process Intensification and Catalysis, in: Reference Module in Chemistry, Molecular Sciences and Chemical Engineering, Elsevier, 2019. Doi: 10.1016/B978-0-12-409547-2.14343-4.

[4] K.S. Suslick, Sonochemistry, Science 247 (1990) (1979) 1439–1445, https://doi.org/10.1126/science.247.4949.1439.

[5] M. Ashokkumar, F. Cavalieri, F.C. Chemat, K. Okitsu, A. Sambandam, K. Yasui, B. Z. Zisu, Handbook of ultrasonics and sonochemistry, springer Singapore, Singapore (2016), https://doi.org/10.1007/978-981-287-278-4.

[6] B. Gielen, J. Jordens, J. Janssen, H. Pfeiffer, M. Wevers, L.C.J. Thomassen, L. Braeken, T. Van Gerven, Characterization of stable and transient cavitation bubbles in a milliflow reactor using a multibubble sonoluminescence quenching technique, Ultrason. Sonochem. 25 (2015) 31–39, https://doi.org/10.1016/j.ultsonch.2014.08.013.

[7] Y. Yao, Y. Pan, S. Liu, Power ultrasound and its applications: a state-of-the-art review, Ultrason. Sonochem. 62 (2020) 104722, https://doi.org/10.1016/j.ultsonch.2019.104722.

[8] T.G. Leighton, The acoustic bubble, Elsevier (1994), https://doi.org/10.1016/B978-0-12-441920-9.X5001-9.

[9] P. Riesz, D. Berdahl, C.L. Christman, Free radical generation by ultrasound in aqueous and nonaqueous solutions, Environ. Health Perspect. 64 (1985) 233–252, https://doi.org/10.1289/ehp.8564233.

[10] Y.T. Didenko, K.S. Suslick, The energy efficiency of formation of photons, radicals and ions during single-bubble cavitation, Nature 418 (2002) 394–397, https://doi.org/10.1038/nature00895.

[11] V. Mišík, P. Riesz, EPR study of free radicals induced by ultrasound in organic liquids II. Probing the Temperatures of Cavitation Regions, Ultrason Sonochem 3 (1996) 25–37, https://doi.org/10.1016/1350-4177(95)00036-4.

[12] J. Collins, T.G. McKenzie, M.D. Nothling, S. Allison-Logan, M. Ashokkumar, G. G. Qiao, Sonochemically initiated RAFT Polymerization in organic solvents, Macromolecules 52 (2019) 185–195, https://doi.org/10.1021/acs.macromol.8b01845.

[13] D.C. Boffito, F. Galli, C. Pirola, C.L. Bianchi, G.S. Patience, Ultrasonic free fatty acids esterification in tobacco and canola oil, Ultrason. Sonochem. 21 (2014) 1969–1975, https://doi.org/10.1016/j.ultsonch.2014.01.026.

[14] L.M.O. Vaz, M.I. Martins, U. Coutinho Filho, V.L. Cardoso, M.H.M. Reis, Ultrasound-assisted transesterification reactions for biodiesel production with sodium zirconate supported in polyvinyl alcohol as catalyst, Environ. Prog. Sustain. Energy 36 (2017) 1262–1267, https://doi.org/10.1002/ep.12571.

[15] A. Taha, E. Ahmed, A. Ismaiel, M. Ashokkumar, X. Xu, S. Pan, H. Hu, Ultrasonic emulsification: an overview on the preparation of different emulsifiers-stabilized emulsions, Trends Food Sci. Technol. 105 (2020) 363–377, https://doi.org/10.1016/j.tifs.2020.09.024.

[16] D. Schieppati, A. Dreux, W. Gao, P. Fatehi, D.C. Boffito, Ultrasound-assisted carboxymethylation of LignoForce Kraft lignin to produce biodispersants, J. Clean. Prod. 366 (2022) 132776, https://doi.org/10.1016/j.jclepro.2022.132776.

[17] D. Schieppati, N.A. Patience, F. Galli, P. Dal, I. Seck, G.S. Patience, D. Fuoco, X. Banquy, D.C. Boffito, Chemical and biological delignification of biomass: a review, Ind. Eng. Chem. Res. 62 (2023) 12757–12794, https://doi.org/10.1021/acs.iecr.3c01231.

[18] S.S. Rashwan, I. Dincer, A. Mohany, Investigation of acoustic and geometric effects on the sonoreactor performance, Ultrason. Sonochem. 68 (2020) 105174, https://doi.org/10.1016/j.ultsonch.2020.105174.

[19] I. Garcia-Vargas, L. Barthe, P. Tierce, O. Louisnard, Simulations of a full sonoreactor accounting for cavitation, Ultrason. Sonochem. 91 (2022) 106226, https://doi.org/10.1016/j.ultsonch.2022.106226.

[20] M. Girard, D. Vidal, F. Bertrand, J.R. Tavares, M.-C. Heuzey, Evidence-based guidelines for the ultrasonic dispersion of cellulose nanocrystals, Ultrason. Sonochem. 71 (2021) 105378, https://doi.org/10.1016/j.ultsonch.2020.105378.

[21] H. Laajimi, K. Fattahi, D.C. Boffito, Numerical investigation of the ultrasound-assisted biodiesel transesterification with a polyalcohol, Chem. Eng. Process. - Process Intesif. 181 (2022) 109139, https://doi.org/10.1016/j.cep.2022.109139.

[22] Y. Son, Y. No, J. Kim, Geometric and operational optimization of 20-kHz probe-type sonoreactor for enhancing sonochemical activity, Ultrason. Sonochem. 65 (2020) 105065, https://doi.org/10.1016/j.ultsonch.2020.105065.

[23] Y. Fang, T. Yamamoto, S. Komarov, Cavitation and acoustic streaming generated by different sonotrode tips, Ultrason. Sonochem. 48 (2018) 79–87, https://doi.org/10.1016/j.ultsonch.2018.05.011.

[24] P.R. Gogate, S. Mujumdar, A.B. Pandit, Sonochemical reactors for waste water treatment: comparison using formic acid degradation as a model reaction, Adv. Environ. Res. 7 (2003) 283–299, https://doi.org/10.1016/S1093-0191(01)00133-2.

[25] S. Manickam, V.N.D. Arigela, P.R. Gogate, Intensification of synthesis of biodiesel from palm oil using multiple frequency ultrasonic flow cell, Fuel Process. Technol. 128 (2014) 388–393, https://doi.org/10.1016/j.fuproc.2014.08.002.

[26] A.V. Prabhu, P.R. Gogate, A.B. Pandit, Optimization of multiple-frequency sonochemical reactors, Chem. Eng. Sci. 59 (2004) 4991–4998, https://doi.org/10.1016/j.ces.2004.09.033.

[27] A. Kumar, P.R. Gogate, A.B. Pandit, Mapping the efficacy of new designs for large scale sonochemical reactors, Ultrason. Sonochem. 14 (2007) 538–544, https://doi.org/10.1016/j.ultsonch.2006.11.005.

[28] S.M.B. Hashemi, M. Akbari, R. Roohi, Y. Phimolsiripol, Thermosonication process of sour cherries: microbial inactivation kinetics, experimental and computational fluid dynamics simulation, Innov. Food Sci. Emerg. Technol. 94 (2024) 103692, https://doi.org/10.1016/j.ifset.2024.103692.

[29] P.R. Gogate, V.S. Sutkar, A.B. Pandit, Sonochemical reactors: important design and scale up considerations with a special emphasis on heterogeneous systems, Chem. Eng. J. 166 (2011) 1066–1082, https://doi.org/10.1016/j.cej.2010.11.069.

[30] M. Hodnett, M.J. Choi, B. Zeqiri, Towards a reference ultrasonic cavitation vessel. Part 1: preliminary investigation of the acoustic field distribution in a 25 kHz cylindrical cell, Ultrason. Sonochem. 14 (2007) 29–40, https://doi.org/10.1016/j.ultsonch.2006.01.003.

[31] J.K. Chu, T.J. Tiong, S. Chong, U.A. Asli, Y.H. Yap, Multi-frequency sonoreactor characterisation in the frequency domain using a semi-empirical bubbly liquid model, Ultrason. Sonochem. 80 (2021) 105818, https://doi.org/10.1016/j.ultsonch.2021.105818.

[32] S. Glegg, W. Devenport, Linear acoustics, in: Aeroacoustics of Low Mach Number Flows, Elsevier, 2017: pp. 49–72. Doi: 10.1016/B978-0-12-809651-2.00003-5.

[33] R. Jamshidi, B. Pohl, U.A. Peuker, G. Brenner, Numerical investigation of sonochemical reactors considering the effect of inhomogeneous bubble clouds on ultrasonic wave propagation, Chem. Eng. J. 189–190 (2012) 364–375, https://doi.org/10.1016/j.cej.2012.02.029.

[34] K.W. Commander, A. Prosperetti, Linear pressure waves in bubbly liquids: Comparison between theory and experiments, J. Acoust. Soc. Am. 85 (1989) 732–746, https://doi.org/10.1121/1.397599.

[35] A. Prosperetti, L.A. Crum, K.W. Commander, Nonlinear bubble dynamics, J. Acoust. Soc. Am. 83 (1988) 502–514, https://doi.org/10.1121/1.396145.

[36] D. Schieppati, M. Mohan, B. Blais, K. Fattahi, G.S. Patience, B.A. Simmons, S. Singh, D.C. Boffito, Characterization of the acoustic cavitation in ionic liquids in a horn-type ultrasound reactor, Ultrason. Sonochem. 102 (2024) 106721, https://doi.org/10.1016/j.ultsonch.2023.106721.

[37] K. Fattahi, E. Robert, D.C. Boffito, Numerical and experimental investigation of the cavitation field in horn-type sonochemical reactors, Chem. Eng. Process. - Process Intesif. 182 (2022) 109186, https://doi.org/10.1016/j.cep.2022.109186.

[38] P. García-Giménez, J.F. Martínez-López, S.T. Blanco, I. Velasco, S. Otín, Densities and isothermal compressibilities at pressures up to 20 MPa of the systems N,N-dimethylformamide or N,N-dimethylacetamide + α,ω-dichloroalkane, J. Chem. Eng. Data 52 (2007) 2368–2374, https://doi.org/10.1021/je700339f.

[39] D. Lide, CRC handbook of chemistry and physics, 2009-2010, 90th ed., CRC Press, 2009.

[40] A. Wahab, S. Mahiuddin, Isentropic compressibility and viscosity of aqueous and methanolic lithium chloride solutions, Can. J. Chem. 80 (2002) 175–182, https://doi.org/10.1139/v02-007.

[41] A. Brotchie, F. Grieser, M. Ashokkumar, Effect of power and frequency on bubble-size distributions in acoustic cavitation, Phys. Rev. Lett. 102 (2009) 084302, https://doi.org/10.1103/PhysRevLett.102.084302.

[42] A. Dehane, S. Merouani, O. Hamdaoui, A. Alghyamah, Insight into the impact of excluding mass transport, heat exchange and chemical reactions heat on the

sonochemical bubble yield: bubble size-dependency, Ultrason. Sonochem. 73 (2021) 105511, https://doi.org/10.1016/j.ultsonch.2021.105511.
[43] G. Servant, J.-L. Laborde, A. Hita, J.-P. Caltagirone, A. Gérard, Spatio-temporal dynamics of cavitation bubble clouds in a low frequency reactor: comparison between theoretical and experimental results, Ultrason. Sonochem. 8 (2001) 163–174, https://doi.org/10.1016/S1350-4177(01)00074-8.
[44] S. Dähnke, K.M. Swamy, F.J. Keil, Modeling of three-dimensional pressure fields in sonochemical reactors with an inhomogeneous density distribution of cavitation bubbles, Ultrason. Sonochem. 6 (1999) 31–41, https://doi.org/10.1016/S1350-4177(98)00026-1.
[45] A.V. Pandit, V.P. Sarvothaman, V.V. Ranade, Estimation of chemical and physical effects of cavitation by analysis of cavitating single bubble dynamics, Ultrason. Sonochem. 77 (2021) 105677, https://doi.org/10.1016/j.ultsonch.2021.105677.
[46] B. Avvaru, A.B. Pandit, Oscillating bubble concentration and its size distribution using acoustic emission spectra, Ultrason. Sonochem. 16 (2009) 105–115, https://doi.org/10.1016/j.ultsonch.2008.07.003.
[47] Comsol AB, Acoustics Module User's Guide, (n.d.).
[48] R. Roohi, S. Baroumand, R. Hosseinie, G. Ahmadi, Numerical simulation of HIFU with dual transducers: the implementation of dual-phase lag bioheat and non-linear westervelt equations, Int. Commun. Heat Mass Transfer 120 (2021) 105002, https://doi.org/10.1016/j.icheatmasstransfer.2020.105002.
[49] K. Hynynen, Demonstration of enhanced temperature elevation due to nonlinear propagation of focussed ultrasound in dog's thigh in vivo, Ultrasound Med. Biol. 13 (1987) 85–91, https://doi.org/10.1016/0301-5629(87)90078-0.
[50] P. Hariharan, M.R. Myers, R.K. Banerjee, HIFU procedures at moderate intensities—effect of large blood vessels, Phys. Med. Biol. 52 (2007) 3493–3513, https://doi.org/10.1088/0031-9155/52/12/011.
[51] K. Rahn, M. Diamantoglou, D. Klemm, H. Berghmans, T. Heinze, Homogeneous synthesis of cellulose p-toluenesulfonates in N,N-dimethylacetamide/LiCl solvent system, die, Angew. Makromol. Chem. 238 (1996) 143–163, https://doi.org/10.1002/apmc.1996.052380113.
[52] Y. Zheng, J. Song, B. Cheng, X. Fang, Y. Yuan, Preparation and flame retardancy of 3-(hydroxyphenylphosphinyl)-propanoic acid esters of cellulose and their fibers, Cellulose 22 (2015) 229–244, https://doi.org/10.1007/s10570-014-0486-x.
[53] Olympus, Vitesse de propagation des ondes ultrasonores dans les matériaux, Https://Www.Olympus-Ims.Com/Fr/Ndt-Tutorials/Thickness-Gauge/Appendices-Velocities/ (n.d.).
[54] P.R. Gogate, A.M. Wilhelm, A.B. Pandit, Some aspects of the design of sonochemical reactors, Ultrason. Sonochem. 10 (2003) 325–330, https://doi.org/10.1016/S1350-4177(03)00103-2.